1 **Tectonic stress controls saucer-shaped sill geometry and emplacement mechanism.**

2

3 R.J. Walker[1*] and S.P.A. Gill[2]

4 [1]University of Leicester, School of Geography, Geology, and the Environment, University Road,

5 Leicester, LE1 7RH, UK.

6 [2]University of Leicester, Department of Engineering, University Road, Leicester, LE1 7RH, UK.

7

8 *Corresponding author: rich.walker@le.ac.uk

9

10 **ABSTRACT**

11 Saucer-shaped sills are common in sedimentary basins worldwide. The saucer shape relates to

12 asymmetric sill-tip stress distributions during intrusion caused by bending of the overburden. Most

13 saucer-shaped sill models are conducted using a magma-analogue excess source-pressure (P_o) to

14 drive host rock failure, but without tectonic stress. Here we present axisymmetric finite element

15 simulations of radially-propagating sills for a range of tectonic stress (σ_r) conditions; from horizontal

16 tension ($\sigma_r < 0$), to horizontal compression ($0 < \sigma_r$). Response to σ_r falls into four regimes, based

17 on sill geometry, and failure mode of the host rock. The regimes are considered in terms of the ratio

18 of tectonic stress versus magma source pressure $R = \sigma_r/P_o$: (I) initially-seeded sills transition to a

19 dike during horizontal extension ($R < 0$); (II) by increasing R from zero towards one (compressive

20 σ_r) sill base length increases and sill incline decreases; (III) where $1 > R > 2$ sill base length

21 relatively decreases and sill incline increases; and (IV) where $R > 2$, sills grow as inclined sheets.

22 Sills in regimes I-III grow dominantly by tensile failure of the host rock, whereas sills in regime IV

23 grow by shear failure of the host rock. Varying σ_r achieves a range of sill geometries that match

24 natural sill profiles. Tectonic stress therefore represents a primary control on saucer-shaped sill

25 geometry and emplacement mechanism.

26

27 **INTRODUCTION**

28 Igneous sills are a major contributor to magma transport through, and storage within, Earth's crust

29 (e.g., Leat, 2008; Muirhead et al., 2014). Observations of natural sills, numerical models for

30 centrally-fed sills emplaced into isotropic elastic media (Malthe-Sorenssen et al., 2004), and

31 laboratory models for sill intrusion (e.g., Galland et al., 2009), show that transgressive saucer-

32 shaped sills are a fundamental geometry in shallow intrusive systems. Such saucer-like geometries

33 are recognized in sedimentary basins worldwide (e.g., Cartwright and Hansen, 2006; Thomson,

34 2007), comprising a relatively flat inner sill that transitions on the periphery to an inward-dipping

35 inclined sheet (e.g., Fig. 1A).

36　　　　Recent studies of inclined (Walker et al., 2017; Stephens et al., 2017,2018) and saucer-

37 shaped sills (Walker, 2016) indicate that sill geometry can be strongly controlled by the tectonic

38 stress state at the time of sill growth. Walker et al., (2017) showed that inclined portions of sills

39 emplaced during episodes of horizontal shortening, record shear displacement across the intrusion,

40 and therefore represent newly-formed magma-filled thrust faults. Most laboratory and numerical

41 models for igneous sill emplacement are conducted without tectonic stress (Kavanagh et al., 2018;

42 see exceptions, e.g., Galland et al., 2003; Bunger et al., 2008; Maccaferri et al., 2011). The rationale

43 for this condition is that although it is recognized that sills correspond to a vertical minimum

44 compressive stress ($\sigma_z = \sigma_3$; here compressive stress is positive, with $\sigma_3 \leq \sigma_2 \leq \sigma_1$) (Anderson,
45 1936, 1951), sills are typically treated as forming by deflection from diking (Gretener, 1969), in
46 response to a local rotation of the stress axes (from horizontal σ_3, to vertical; e.g., Gudmundsson,
47 2011). Deflection is typically considered to relate to host rock layer heterogeneity (Kavanagh et al.,
48 2006; Gudmundsson, 2011); not a far-field tectonic stress (Roberts, 1970). Laboratory models
49 (Galland et al., 2009; Galland and Scheibert, 2013) and numerical simulations for sill growth (Malthe-
50 Sorenssen et al., 2004), and for static sill-induced fracture (Haug et al., 2017, 2018), under initially
51 lithostatic conditions feature a transition from a flat intrusion to a steeply inclined sheet (typically
52 $\geq 25°$; Fig. 1B), with a concave downward incline form. However, natural examples of saucer-
53 shaped sills may be concave upward in profile, and have a much wider range of inclines (including
54 $< 25°$; Fig. 1B).

55   Modelled inclines in the literature (Fig. 1B) are the result of elastic bending of the
56 overburden (Malthe-Sorenssen et al., 2004), or shear failure of the host material induced by a
57 blunted sill tip (Haug et al., 2017). Elastic bending above the sill results in an asymmetric stress
58 concentration at the sill tip, favouring inclined propagation at some critical sill radius (r_c) relative to
59 the initial emplacement depth (H). Typically, r_c is $1H$ to $2H$ in models, but can be $> 3H$ in nature
60 (see Fig. 1B). In contrast, laboratory sill experiments in elastic media performed by Bunger et al.,
61 (2008) showed that the effect of asymmetric stress distribution ahead of the sill tip can be opposed
62 by applying horizontal (radial) shortening, producing flatter sills as a function of increasing
63 horizontal compression (Fig. 1B).

64   Here we use finite element (FE) simulations to demonstrate the importance of the ambient
65 stress state in controlling saucer-shaped sill geometry during growth, and reconcile the difference
66 between modelled geometries and those in nature. Further, we demonstrate that the mechanism
67 of sill emplacement is fundamentally controlled by the ambient stress.

68

69 **METHODS**
70 We implemented an axisymmetric FE model of sill propagation, incorporating coupled processes of
71 linear elastic deformation of the host rock, damage mechanics for rock fracture, and fluid flow for
72 magma movement, in COMSOL Multiphysics (v5.3). The full model domain is 8 km deep with radius
73 16 km; the region of interest consists of linear 4-noded square elements with an initial side length
74 (w_0) of 20 m (Fig. 2A,B). Horizontal sills of height w_0 and length $5w_0$ are seeded at a vertical depth
75 (H) of 1 km below the free surface. We apply a linear shape function to the crack band damage
76 model (Mazars and Pijaudier-Cabot, 1989) so that non-physical stresses are not resolved at the
77 square corners of the modelled sill tip (Gill and Walker, 2020). The Young's modulus (E_0) of the rock
78 is 1 GPa, with a Poisson's ratio (ν) of 0.4. Magma viscosity (μ) is constant at 10^6 Pa·s and the Bulk
79 Modulus of the magma (K_f) is 0.1 GPa. The rock density (ρ_r) is 2.5 g/cm^3 and the magma density
80 (ρ_m) is 2.3 g/cm^3. Accounting for the rock density, at depth $z = H$ the vertical stress σ_z and
81 lithostatic stress (P_L, here also considered hydrostatic, where $\sigma_1 = \sigma_3$) is ~25 MPa (where $P_L =$
82 $\rho_r g z$, and $g = 9.81 m/s^2$ is the acceleration due to gravity). Two failure criteria for the host rock
83 are implemented: (1) mode I tensile failure, which occurs when $\sigma_3 = \sigma_T = -3 MPa$, the tensile
84 strength of the rock; and (2) Mohr-Coulomb shear failure, with shear failure stress $\tau_f = \sigma_n tan\phi +$
85 C, where σ_n is the normal stress on the failure plane, $C = 20 MPa$ is the material shear cohesion,

86 and $\phi = 30°$ is the angle of internal friction for the host material. Horizontal radial stress σ_∞ is
87 applied to the external boundary of the model to simulate tectonic stress (Fig. 2A). We will refer to
88 the differential horizontal stress $\sigma_r = \sigma_\infty - P_L$: σ_r is zero when the state of stress is lithostatic,
89 negative in tension ($\sigma_\infty < \sigma_z$), and positive in compression ($\sigma_\infty > \sigma_z$).

90   The exact criteria for intrusion propagation are not well known as they depend on the local
91 conditions at the propagation front, such as the sharpness of the tip. Sill propagation in the model
92 is achieved by applying a constant magma flux, with source overpressure $P_o = 5MPa$ applied at
93 $(r, z) = (0, H)$. P_o is excess to P_L, and is the reference state for other stress measures in the model.
94 P_o decays along the sill with naturally developing pressure gradients driving magma flow from the
95 source to the tip (Gill and Walker, *2020*). Bunger et al., (2008) introduced a dimensionless parameter
96 χ as a means to define scale-independent factors affecting sill profiles (Fig. 1B): $\chi = \sigma_r\sqrt{H}/K_c$. The
97 fracture toughness in the FE model is calculated from the energy release rate: $G_c = \frac{K_c^2}{E_0}$, where $G_c =$
98 $\frac{dU}{dA}$; U is the total change in energy and A is the crack area. This yields $K_c^{FE} = 26MPa\sqrt{m}$, and allows
99 comparison with results from Bunger et al., (2008); the FE superscript denotes that this is simulation
100 parameter, dependent on the model, and not a physical parameter. We find in the model that the
101 magma pressure distribution evolves to keep the stress intensity K constant at the tip, so that $K =$
102 K_C. Sill growth in our models is therefore controlled by the toughness of the rock. Further details
103 about the model, and the effect of changing ψ is investigated in Gill and Walker (*2020*).

104

105 **RESULTS**
106 Figures 2 and 3 show results and summary profiles for sills across the range of σ_r studied here. Sill
107 growth behaviour can be divided into four regimes as a function of the ratio $R = \sigma_r/P_o$ (Fig. 4): (I)
108 horizontal tension ($R < 0$), results in an abrupt transition of the initial sill to a near-vertical dike (Fig.
109 3A); (II) $0 < R < 1$ results in a decrease in sill incline and increase in sill base length (Fig. 3A); (III)
110 $1 < R < 2$, results in flat sills; and (IV) > 2 results in increased sill inclines and short base lengths
111 (Fig. 3B). Sills in regimes I-III are emplaced by tensile failure of the host rock (Fig. 2C-G), with regime
112 III showing minor extensional shear failure. Sills in regime IV are emplaced solely by Mohr-Coulomb
113 failure of the host rock (Fig. 2H-K). Transition in failure mode begins at $\sigma_r = 10MPa$, with full
114 transition at $11MPa$.

115   The modelled sills show a transition in profile geometry, from concave downward for $-1.2 \leq$
116 $\sigma_r \leq 2.4\ MPa$, to concave upward profiles for $\sigma_r < 2.4\ MPa$. Notably, most laboratory models
117 (e.g., Galland et al., 2009) and numerical simulations (e.g., Malthe-Sorenssen et al, 2004; Haug et
118 al., 2017) produce concave downward incline profiles, but many natural sill inclines are concave
119 upward (e.g. Fig. 1). The effect of σ_r on sill shape, in terms of the critical base length r_c and incline
120 θ, is summarised in Figure 4. Sills in regime I show the shortest base lengths ($< 0.5H$), with r_c
121 reaching its maximum ($\sim 4.5H$) at the regime II-III transition.

122

123 **DISCUSSION**
124 Horizontal stress has a pronounced effect on intrusion geometry and host rock failure mechanism
125 (Fig. 4). Horizontal tension causes initially-seeded sills to transition to dikes. At $\sigma_r = 0$, the sill climbs
126 at ~25°, and by σ_r = 5 MPa, this is reduced to ~1° (Fig. 4). The incline of the sill relates to bending of
127 the overburden, which preferentially induces tensile stress above the sill tip (Malthe-Sorenssen et

128   al, 2004). Stress is additive, and increasing compressive σ_r subdues this asymmetry, promoting a
129   flatter sill. Normalising sill dimensions to the original depth H allows comparison of the modelled
130   sills with natural examples (Fig. 3; see also Bunger et al., 2008). Results at the lower stress range of
131   regime II compare favourably with scaled laboratory model results of Bunger et al. (2008) (Fig. 4).
132   Sills in regime III show a good fit to the natural saucer-shaped sills shown in Figures 1 and 3; models
133   where $\sigma_r = 0$ show a very poor fit with the natural examples (Fig. 1B and 3). In regime IV, large σ_r
134   results in a short sill base (r_c) and an increase in sill incline (θ) similar to saucer-shaped sills emplaced
135   during identified phases of horizontal tectonic shortening (e.g., the Stremoy Sill, shown in Figure 1;
136   Walker, 2016).
137   At distance from the sill, a tectonic stress of σ_r generates a maximum shear stress τ_{max} of
138    $\frac{1}{2}|\sigma_r|$ at 45° to the horizontal (**Fig. 2A**). The propagation of the sill through this stressed medium is
139   complex, as it is controlled by the localised stresses generated at the sill tip due to the pressurised
140   magma interacting with σ_r. The larger the value of σ_r, the larger the shear stress τ experienced at
141   the growing sill tip, increasing the likelihood of failure in shear (e.g., Sibson, 1998; Ramsey and
142   Chester, 2004). The Mohr-Coulomb failure criterion starts to become important in regime III of our
143   simulations, though failure is still dominated by σ_T. In regime IV the intrusion is accommodated
144   entirely by shear fracture in the host rock, despite the 20 MPa shear cohesion of the material.
145   Previous studies have highlighted the potential for sills to resolve a component of shear within the
146   plane (Walker, 2016; Walker et al., 2017; Stephens et al., 2017, 2018; Coetzee et al., 2019) as part
147   of an extensional-shear conjugate array, in cases where σ_r is relatively large ($> 4\sigma_T$). Walker et al.,
148   (2017) also showed that inclined sills can also represent magma-filled reverse faults. Shear across
149   the modelled intrusions here is largely controlled by their incline. The resolved shear stress on the
150   sill plane is $\tau = \frac{\sigma_r}{2}\sin 2\theta$, hence even at very large values for σ_r, a near-horizontal or near-vertical
151   plane experiences very low τ. In our models, τ becomes significant (>2 MPa) on inclined sill planes
152   where $\sigma_r \geq 11 MPa$ because this coincides with an increase in sill incline to $\theta > 10°$; modelled sills
153   emplaced where $\sigma_r \geq 11 MPa$ therefore represent magma-filled extensional shear faults on the
154   inclined segments (Fig. 2I), rather than simple hydrofractures.
155   Magnitudes of stress in the simulations are relative to the magma overpressure P_o required
156   to induce failure at the tip. The modelled sills are rectangular in section, rather than bladed or
157   elliptical geometries which are common in nature, and in models for dikes (Pollard et al., 1975;
158   Mastin and Pollard, 1988; Rivalta et al., 2015). The rectangular tip requires a greater magnitude of
159   P_o to facilitate propagation, than would be the case for sharp or bladed tips (Vachon and
160   Hieronymus, 2017). Bladed geometries that propagate in mode I result in a maximum stress
161   concentration that is in plane with the intrusion (Rubin and Pollard, 1988; Maccaferri et al., 2010).
162   Sharp tips also efficiently focus the stress concentration ahead of the tip, leading to failure at low
163   applied stresses. Our modelled tips are blunt, which is less efficient at concentrating stress. Tip
164   bluntness also has the effect of offsetting the maximum stress concentration from in-plane, to the
165   positions of maximum tip curvature, i.e., the corners of a rectangular tip (Greenspan, 1944; Poppe
166   et al., 2019); as noted though, such non-physical stresses are processed-out of our modelled sill tips.
167   In a dike model, tip blunting could result in different deformation styles above shallow intrusions
168   (Poppe et al., 2020); extensional grabens above bladed dikes (Mastin and Pollard, 1988), versus fold-
169   and-thrust systems above rectangular tips (Wyrick and Smart, 2009). In a sill model, tip-blunting can

170 lead to a piston-like effect, in which the intrusion can never propagate in plane (e.g., Haug et a.,
171 2017). In such a case, the sill would grow in thickness rather than radially, causing the overburden
172 to be jacked up vertically, and inducing shear faults at the periphery. Accurately modelling the tip
173 geometry, including as it evolves with changes to the host rock properties and magma viscosity, is
174 therefore an important future target for scaled intrusion modelling.
175

176 **CONCLUSIONS**
177 The magnitude of horizontal compressive stress is a primary control on saucer-shaped sill geometry.
178 Minor compressive stress produces flatter sills that grow for long distances without climbing toward
179 the surface. Larger tectonic stress promotes a transition from extension-fracture dominance to
180 shear-fracture dominance; not all sills represent extension-mode fractures. The observed range in
181 natural saucer-shaped sill geometries may represent the tectonic stress state during their
182 emplacement, presenting a potential tool for constraining regional stress states, particularly where
183 other diagnostic structures may not be resolved.
184

189 **REFERENCES**
190 Anderson, E. M., 1936 The dynamics of the formation of cone sheets, ring dykes and cauldron
191   subsidence, Proc. Roy. Soc. Edinburgh, 56, 128-163
192 Anderson, E.M., 1951. The dynamics of faulting and dyke formation with applications to Britain,
193   Hafner Pub. *Co., Oliver and Boyd, London*.
194 Bunger, A.P., Jeffrey, R.G. and Detournay, E., 2008. Evolution and morphology of saucer-shaped
195   sills in analogue experiments. Geological Society, London, Special Publications, 302(1),
196   pp.109-120.
197 Cartwright, J. and Møller Hansen, D., 2006. Magma transport through the crust via interconnected
198   sill complexes. Geology, 34(11), pp.929-932.
199 Coetzee, A., Kisters, A.F.M. and Chevallier, L., 2019. Sill complexes in the Karoo LIP: Emplacement
200   controls and regional implications. Journal of African Earth Sciences, p.103517.
201 Galland, O. and Scheibert, J., 2013. Analytical model of surface uplift above axisymmetric flat-lying
202   magma intrusions: Implications for sill emplacement and geodesy. Journal of Volcanology
203   and Geothermal Research, 253, pp.114-130.
204 Galland, O., Planke, S., Neumann, E.R. and Malthe-Sørenssen, A., 2009. Experimental modelling of
205   shallow magma emplacement: Application to saucer-shaped intrusions. Earth and Planetary
206   Science Letters, 277(3-4), pp.373-383.
207 Gill, S. P. A., & Walker, R. J. (2020). The roles of elastic properties, magmatic pressure, and tectonic
208   stress in saucer-shaped sill growth. Journal of Geophysical Research: Solid Earth, 124,
209   e2019JB019041. https://doi.org/ 10.1029/2019JB019041
210 Greenspan, M., 1944. Effect of a small hole on the stresses in a uniformly loaded plate. *Quarterly*
211   *of Applied Mathematics*, *2*(1), pp.60-71.

212   Gudmundsson, A., 2011. Deflection of dykes into sills at discontinuities and magma-chamber
213   formation. Tectonophysics, 500(1-4), pp.50-64.

214   Hansen, J. 2011. Petrogenetic Evolution, Geometries and Intrusive Styles of the Early Cenozoic
215   Saucer-Shaped Sills of the Faroe Islands. Doctoral thesis, Durham University.

216   Haug, Ø.T., Galland, O., Souloumiac, P., Souche, A., Guldstrand, F. and Schmiedel, T., 2017.
217   Inelastic damage as a mechanical precursor for the emplacement of saucer-shaped
218   intrusions. Geology, 45(12), pp.1099-1102

219   Haug, Ø.T., Galland, O., Souloumiac, P., Souche, A., Guldstrand, F., Schmiedel, T. and Maillot, B.,
220   2018. Shear Versus Tensile Failure Mechanisms Induced by Sill Intrusions: Implications for
221   Emplacement of Conical and Saucer-Shaped Intrusions. Journal of Geophysical Research:
222   Solid Earth, 123(5), pp.3430-3449.

223   Kavanagh, J.L., Menand, T. and Sparks, R.S.J., 2006. An experimental investigation of sill formation
224   and propagation in layered elastic media. Earth and Planetary Science Letters, 245(3-4),
225   pp.799-813.

226   Kavanagh, J.L., Engwell, S.L. and Martin, S.A., 2018. A review of laboratory and numerical
227   modelling in volcanology. *Solid Earth*, *9*(2), pp.531-571.

228   Leat, P.T., 2008. On the long-distance transport of Ferrar magmas. Geological Society, London,
229   Special Publications, 302(1), pp.45-61.

230   Maccaferri, F., Bonafede, M. and Rivalta, E., 2010. A numerical model of dyke propagation in
231   layered elastic media. Geophysical Journal International, 180(3), pp.1107-1123.

232   Malthe-Sørenssen, A., Planke, S., Svensen, H., Jamtveit, B., Breitkreuz, C. and Petford, N., 2004.
233   Formation of saucer-shaped sills. Physical geology of high-level magmatic systems.
234   Geological Society, London, Special Publications, 234, pp.215-227.

235   Mastin, L.G. and Pollard, D.D., 1988. Surface deformation and shallow dike intrusion processes at
236   Inyo Craters, Long Valley, California. Journal of Geophysical Research: Solid Earth, 93(B11),
237   pp.13221-13235

238   Mazars, J and Pijaudier-Cabot, G, 1989. Continuum Damage Theory —Application to Concrete,
239   *Journal of Engineering Mechanics*, 115, 345-65

240   Muirhead, J.D., Airoldi, G., White, J.D. and Rowland, J.V., 2014. Cracking the lid: Sill-fed dikes are
241   the likely feeders of flood basalt eruptions. Earth and Planetary Science Letters, 406, pp.187-
242   197.

243   Pollard, D.D., Muller, O.H. and Dockstader, D.R., 1975. The form and growth of fingered sheet
244   intrusions. Geological Society of America Bulletin, 86(3), pp.351-363.

245   Poppe, S., Holohan, E.P., Galland, O., Buls, N., Van Gompel, G., Keelson, B., Tournigand, P.Y.,
246   Brancart, J., Hollis, D., Nila, A. and Kervyn, M., 2019. An Inside Perspective on Magma
247   Intrusion: Quantifying 3D Displacement and Strain in Laboratory Experiments by Dynamic X-
248   Ray Computed Tomography. Frontiers in Earth Science, 7, p.62.

249   Poppe, S., Galland, O., de Winter, N.J., Goderis, S., Claeys, P., Debaille, V., Boulvais, P. and Kervyn,
250   M., 2020. Structural and geochemical interactions between magma and sedimentary host
251   rock: the Hovedøya case, Oslo Rift, Norway. *Geochemistry, Geophysics, Geosystems*.

252   Ramsey, J.M. and Chester, F.M., 2004. Hybrid fracture and the transition from extension fracture
253   to shear fracture. Nature, 428(6978), p.63.

254 Rivalta, E., Taisne, B., Bunger, A.P. and Katz, R.F., 2015. A review of mechanical models of dike
255   propagation: Schools of thought, results and future directions. Tectonophysics, 638, pp.1-42.
256 Rubin, A.M. and Pollard, D.D., 1988. Dike-induced faulting in rift zones of Iceland and
257   Afar. Geology, 16(5), pp.413-417.
258 Sibson, R.H., 1998. Brittle failure mode plots for compressional and extensional tectonic
259   regimes. Journal of Structural Geology, 20(5), pp.655-660.
260 Stephens, T.L., Walker, R.J., Healy, D., Bubeck, A., England, R.W. and McCaffrey, K.J., 2017. Igneous
261   sills record far-field and near-field stress interactions during volcano construction: Isle of
262   Mull, Scotland. Earth and Planetary Science Letters, 478, pp.159-174.
263 Stephens, T.L., Walker, R.J., Healy, D., Bubeck, A. and England, R.W., 2018. Mechanical models to
264   estimate the paleostress state from igneous intrusions. Solid earth.
265 Thomson, K., 2007. Determining magma flow in sills, dykes and laccoliths and their implications for
266   sill emplacement mechanisms. Bulletin of Volcanology, 70(2), pp.183-201.
267 Vachon, R. and Hieronymus, C.F., 2016. Effect of host-rock rheology on dyke shape, thickness and
268   magma overpressure. Geophysical Journal International, 208(3), pp.1414-1429.
269 Walker, R.J., 2016. Controls on transgressive sill growth. Geology, 44(2), pp.99-102
270 Walker, R.J., Healy, D., Kawanzaruwa, T.M., Wright, K.A., England, R.W., McCaffrey, K.J.W., Bubeck,
271   A.A., Stephens, T.L., Farrell, N.J.C. and Blenkinsop, T.G., 2017. Igneous sills as a record of
272   horizontal shortening: The San Rafael subvolcanic field, Utah. GSA Bulletin, 129(9-10),
273   pp.1052-1070.
274 Wyrick, D.Y., and Smart, K.J., 2009a, Dike-induced deformation and Martian graben systems:
275   Journal of Volcanology and Geothermal Research, v. 185, p. 1–11,
276   doi:10.1016/j.jvolgeores.2008.11.022.
277
278 **FIGURES**
279 **Fig. 1.** Saucer-shaped sill geometry in nature and in models from published examples. **(A)** The
280 Streymoy sill, Faroe Islands shows a flat inner region, which transitions to an inward-dipping
281 periphery. Sill dips are from Hansen (2011). **(B)** Normalised plots of modelled sill profiles (Bunger et
282 al., 2008; Galland et al., 2009; Haug et al., 2017), and natural sills (Galland et al., 2009). H is initial
283 depth of intrusion, z is depth, and r is intrusion radius. Galland et al., (2009) used silica powder and
284 vegetable oil for the host rock and magma analogues, respectively. Bunger et al., (2008) used glass
285 or PMMA, and water. They also introduced a dimensionless parameter χ, where $\chi = \sigma_r \sqrt{H}/K_c$. K_c
286 is 1.3 and 0.6 MPa m$^{1/2}$ for their PMMA and glass respectively. Haug et al., (2017) used a rigid-
287 plasticity approach to simulate sills in a homogenous Mohr-Coulomb material. The 'sills' in their
288 models did not grow in length; individual plots show the damage associated with cracks of variable
289 starting length. Starting depth H was 2 km, and sill thickness was 50 m, with a blunt tip region.
290
291 **Fig. 2.** Model set-up and examples of simulation results. **(A-B)** Model domain consists of an
292 unstructured mesh to move boundaries far from the sills, with a square-noded grid in the region of
293 the sills (within the yellow box). Models are axisymmetric about the blue line. **(C-K)** Simulation
294 results for variable σ_r. Each plot shows change in stress $\Delta\sigma_r$, and the principal strain axes for
295 maximum and minimum elongation. Note that for hydrofractures (extension mode), the principal
296 strain axes should coincide with the principal axes of the sill plane (e.g., C-F); strain axes in the region

297   of the sill that are not parallel or orthogonal to the sill plane therefore represent oblique opening
298   (extensional shear; e.g., G-K). The sill is color-coded for tensile failure (red) and Mohr-Coulomb
299   failure (orange) within the host rock: Note the transition from tensile failure dominance to shear
300   failure dominance, from 10-11 MPa.

301

302   **Fig. 3.** Normalised intrusion profiles as a function of σ_r. **(A)** Tensile to mildly-compressive σ_r. **(B)**
303   Strongly-compressive σ_r. See Figure 1 for details of χ. Note that the steps in the profiles are an
304   artefact of the model mesh.

305

306   **Fig. 4.** Summary of results for **(A)** sill base length and **(B)** sill incline angle θ for the studied range of
307   σ_r. Grey regions show the range of χ values for the scaled laboratory models of Bunger et al., (2008);
308   results from their PMMA and glass experiments are also shown.
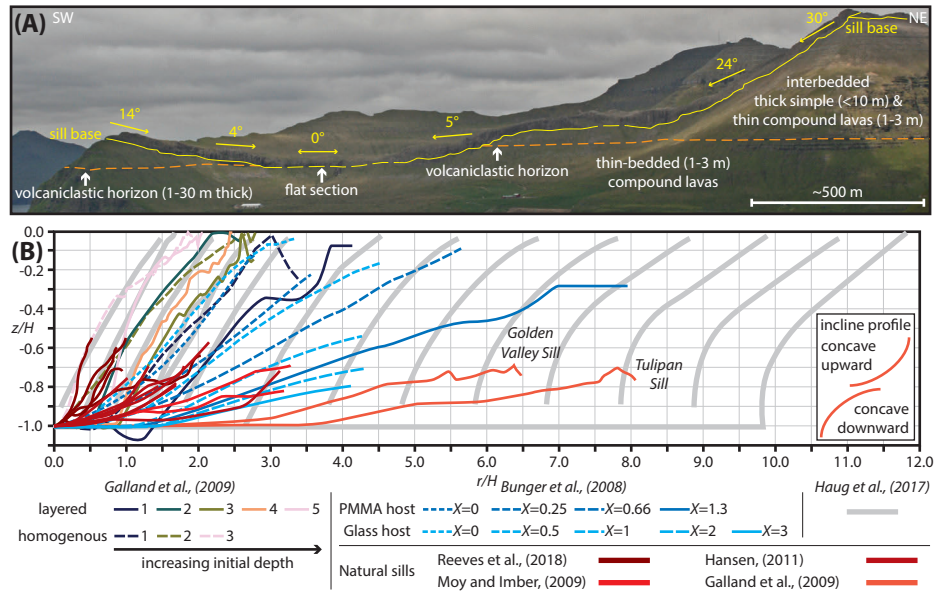
Figure 1
W = 122 mm
H = 75 mm
(2 column, colour)

Fig. 1. Saucer-shaped sill geometry in nature and in models from published examples. (A) The Streymoy sill, Faroe Islands shows a flat inner region, which transitions to an inward-dipping periphery. Sill dips are from Hansen (2011). (B) Normalised plots of modelled sill profiles (Bunger et al., 2008; Galland et al., 2009; Haug et al., 2017), and natural sills (Galland et al., 2009). H is initial depth of intrusion, z is depth, and r is intrusion radius. Galland et al., (2009) used silica powder and vegetable oil for the host rock and magma analogues, respectively. Bunger et al., (2008) used glass or PMMA, and water. They also introduced a dimensionless parameter χ, where $\chi = \sigma_r \sqrt{H}/K_c$. K_c is 1.3 and 0.6 MPa m1/2 for their PMMA and glass respectively. Haug et al., (2017) used a rigid-plasticity approach to simulate sills in a homogenous Mohr-Coulomb material. The 'sills' in their models did not grow in length; individual plots show the damage associated with cracks of variable starting length. Starting depth H was 2 km, and sill thickness was 50 m, with a blunt tip region.
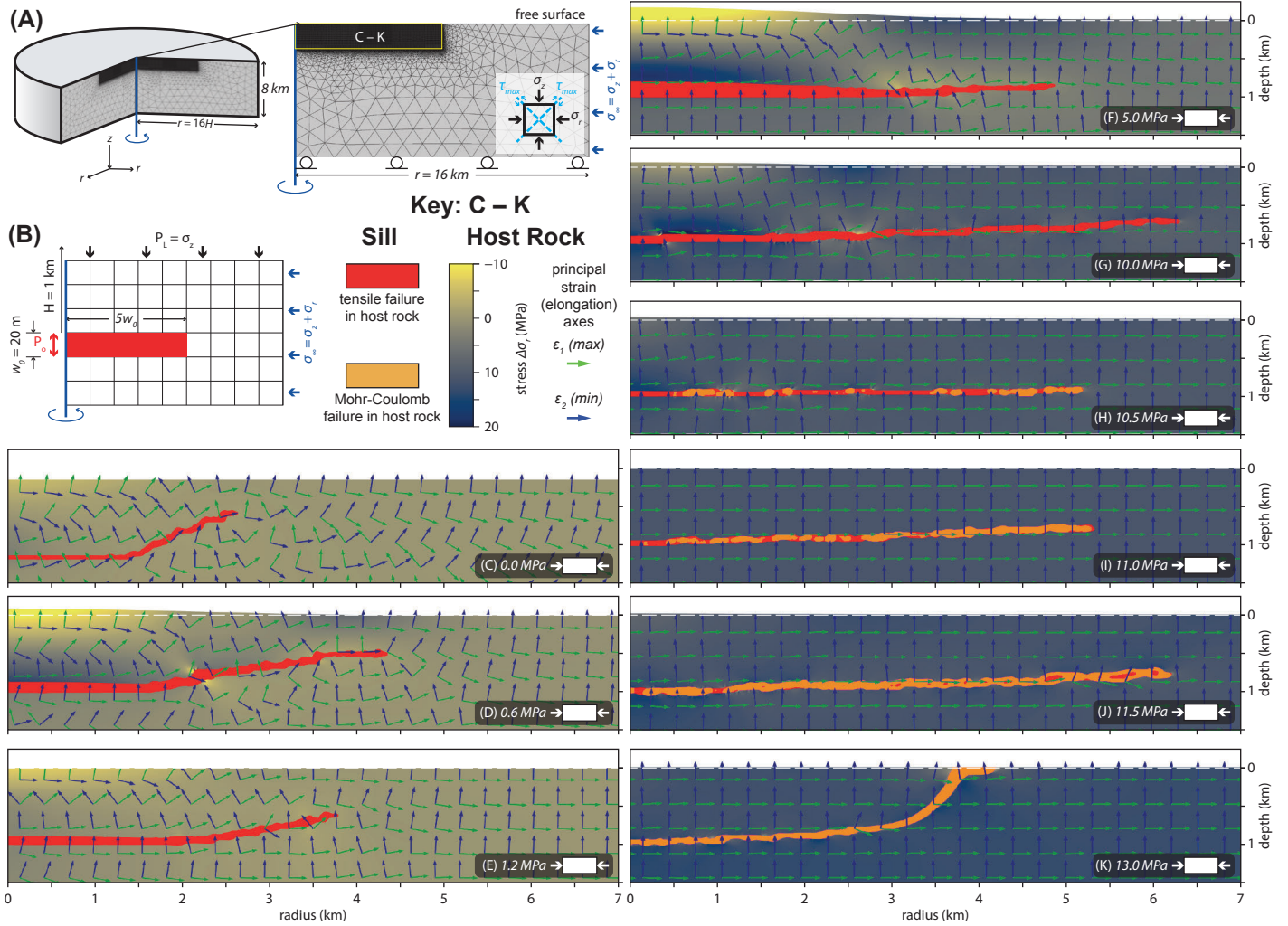
Fig. 2. Model set-up and examples of simulation results. (A-B) Model domain consists of an unstructured mesh to move boundaries far from the sills, with a square-noded grid in the region of the sills (within the yellow box). Models are axisymmetric about the blue line. (C-K) Simulation results for variable σ_r. Each plot shows change in stress $[\![\Delta\sigma]\!]\_r$, and the principal strain axes for maximum and minimum elongation. Note that for hydrofractures (extension mode), the principal strain axes should coincide with the principal axes of the sill plane (e.g., C-F); strain axes in the region of the sill that are not parallel or orthogonal to the sill plane therefore represent oblique opening (extensional shear; e.g., G-K). The sill is color-coded for tensile failure (red) and Mohr-Coulomb failure (orange) within the host rock: Note the transition from tensile failure dominance to shear failure dominance, from 10-11 MPa.
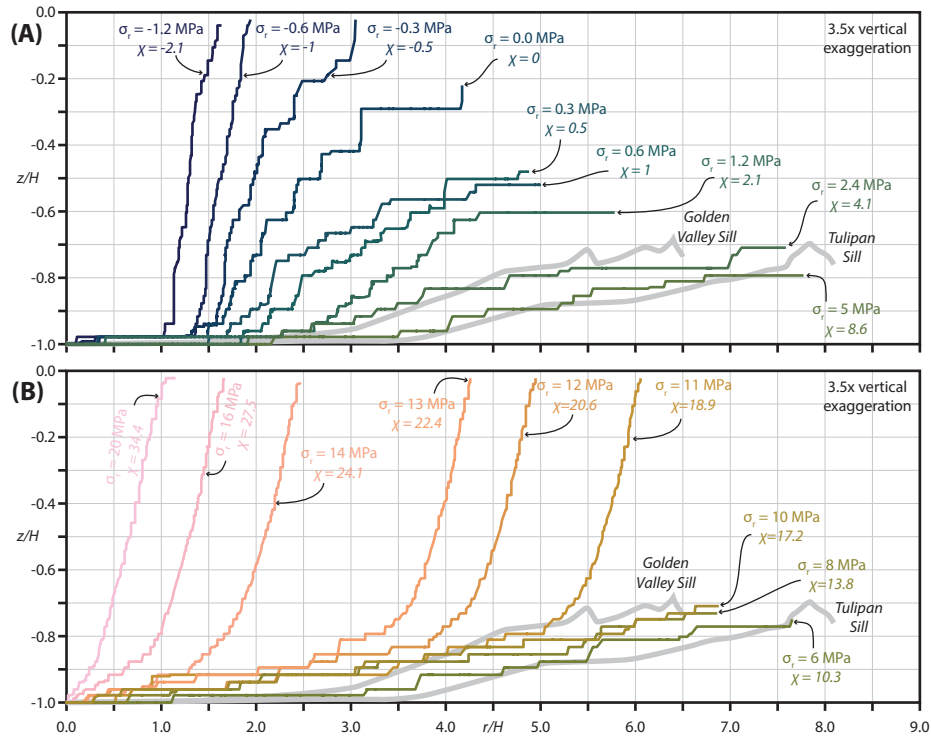
Figure 3
W = 122 mm
H = 97 mm
(2 column, colour)

Fig. 3. Normalised intrusion profiles as a function of σ_r. (A) Tensile to mildly-compressive σ_r. (B) Strongly-compressive σ_r. See Figure 1 for details of X. Note that the steps in the profiles are an artefact of the model mesh.

Figure 4
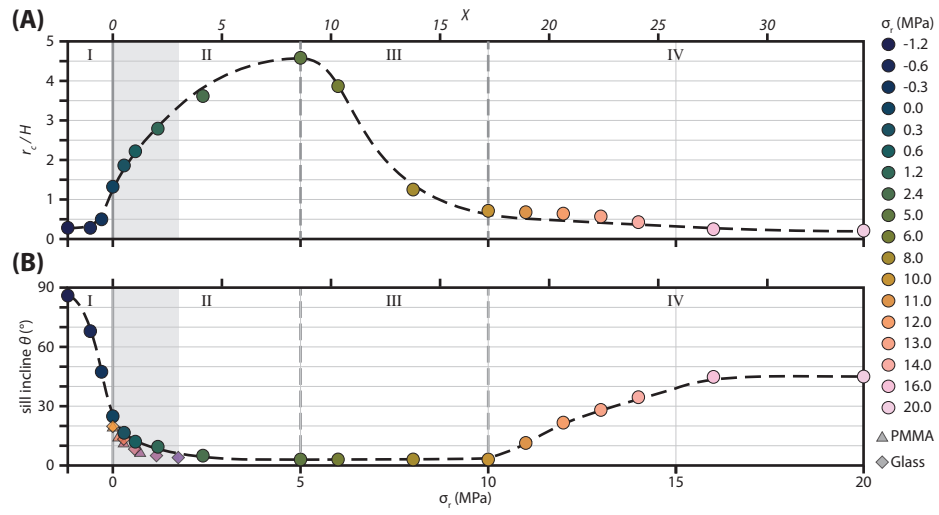**W = 122 mm**
H = 68 mm
(2 column, colour)

Fig. 4. Summary of results for (A) sill base length and (B) initial sill incline angle θ for the studied range of σ_r. Grey regions show the range of X values for the scaled analogue laboratory models of Bunger et al., (2008); results from their PMMA and glass experiments are also shown.